An optimal volumetric constraint ratio with implementation using mixed FE-Meshfree formulation

Wu Junchao[a,*], Chu Yingjie[1], Xu Yangtao[a], Wang Dongdong[1]

[a] *Key Laboratory for Intelligent Infrastructure and Monitoring of Fujian Province, College of Civil Engineering, Huaqiao University , Xiamen, Fujian, 361021, China*

Abstract

Formulations for incompressible materials often suffer from volumetric locking, leading to reduced accuracy and oscillatory displacement and pressure solutions. A well-chosen constraint ratio can mitigate this issue, but traditional approaches lack a theoretical foundation based on the inf-sup (or LBB) condition, which is essential for the stability of mixed formulations. This paper introduces a novel optimal constraint ratio derived from the inf-sup condition to address volumetric locking. The inf-sup test, a numerical tool for verifying the inf-sup condition, is reaffirmed as equivalent to inf–sup condition through a variational approach. By incorporating a complete polynomial space whose dimension matches the number of displacement degrees of freedom (DOFs), a new inf-sup value estimator is developed, explicitly considering the constraint ratio. For a given number of displacement DOFs, ensuring that the pressure DOFs remain below a stabilized number falls within the optimal constraint ratio range can satisfy the inf-sup condition. To implement of optimal constraint ratio, a mixed finite element and meshfree formulation is proposed, where displacements are discretized using traditional finite element approximations, and pressures are approximated via the reproducing kernel meshfree method. Leveraging the globally smooth reproducing kernel shape functions, the constraint ratio can be flexibly adjusted to meet the inf-sup condition without the limit of element. For computational efficiency and ease of implementation, pressure nodes are placed on selected displacement nodes to maintain the optimal constraint ratio. Inf-sup tests and a series of 2D and 3D elasticity examples validate the proposed constraint ratio, demonstrating its effectiveness in eliminating volumetric locking and enhancing the performance of mixed finite element and meshfree formulations.

Keywords: Optimal constraint ratio, Inf–sup condition estimator, Volumetric locking, Mixd formulation, Reproducing kernel meshfree approximation

*Corresponding author
Email address: `jcwu@hqu.edu.cn` (Wu Junchao)

1. Introduction

The volumetric constraint is a necessary condition in the formulation of incompressible materials like rubber and hydrogel. Proper imposition of this constraint is crucial for obtaining better numerical solutions; insufficient or excessive constraints will reduce the accuracy and stability of the solution [1]. The volumetric constraint ratio [2], denoted as r, is often used to measure the level of constraint. It is defined as the total degrees of freedom (DOFs) of displacement divided by the total DOFs of pressure. Ideally, the optimal constraint ratio should be consistent with its governing partial differential equations. For example, in the two-dimensional (2D) case, the optimal constraint ratio is 2, since there are two governing equations for displacement and one for pressure. When the constraint ratio is less than 2, the formulation suffers from volumetric locking, while a constraint ratio greater than 2 can cause a coarse solution for pressure. These observations have been summarized by pioneering work [2] as follows:

$$r = \frac{2n_u}{n_p}, \quad \begin{cases} r > 2 & \text{too few constraints} \\ r = 2 & \text{optimal} \\ r < 2 & \text{too many constraints} \\ r \leq 1 & \text{severe locking} \end{cases} \tag{1}$$

where n_u and n_p are the number of control nodes for displacement and pressure, respectively. Classifying the locked status via the constraint ratio is straightforward but imprecise. For instance, the constraint ratio can remain 2 while the pressure is discretized using continuous shape functions identical to the displacement's approximation. However, volumetric locking still exists in this formulation [2].

The inf–sup condition, also known as the Ladyzhenskay–Babuška–Brezzi (LBB) condition [3, 4], is a more precise requirement for a locking–free formulation. This condition is based on the mixed formulation framework, and when the inf–sup condition is satisfied, both the accuracy and stability of the mixed-formulation can be ensured. However, verifying the inf–sup condition is non-trivial. An eigenvalue problem namely inf–sup test can be used to check this condition numerically [5, 6, 7, 8]. Analytically, Brezzi and Fortin proposed a two-level projection framework that always satisfies the inf-sup condition, allowing it to be checked by identifying whether the formulation is included in this framework. Both analytical and numerical methods to check the inf-sup condition are complex, and the relationship between the constraint ratio and the inf-sup condition remains unclear.

To address volumetric constraint issues, adjusting the constraint ratio to an appropriate level is commonly used and easily implemented. In traditional finite element methods (FEM), this adjustment is carried out based on elements since the DOFs are embedded in each element. Conventional FEM often exhibits an over–constrained status. Reducing the approximation order of pressure in mixed formulation can alleviate the constraint burden, such as with the well-known Q4P1 (4–node quadrilateral displacement element with 1–node piecewise constant pressure element) and Q8P3. Globally, using continuous shape functions to link the local pressure DOFs in each element can also reduce the total number of pressure DOFs and increase the constraint ratio, such as with T6P3 (6–node triangular displacement element with 3–node continuous linear pressure element) and Q9P4 (Taylor–Hood element) [9]. These schemes belong to the mixed formulation framework and can also be implemented through a projection approach, where the pressure approximant is projected into a lower–dimensional space. Examples include selective integration methods [10, 11], B–bar or F–bar methods [12, 13, 14, 15, 16], pressure projection methods [17, 18], and the enhanced strain method [19]. Meanwhile, conventional 3–node triangular elements arranged in a regular cross pattern can also reduce the dimension of the pressure space [20]. It should be noted that not all of these methods can meet the inf–sup condition despite alleviating volumetric locking and producing a good displacement solution. Some methods, like Q4P1, show significant oscillation for the pressure solution, known as spurious pressure mode or checkerboard mode [20]. In such cases, additional stabilization approaches, such as multi-scale stabilization (VMS) [21, 22, 23, 24] or Galerkin/least-squares (GLS) [25], are required to eliminate the oscillations in pressure.

Another class of FEM methods adjusts the constraint ratio by increasing the displacement DOFs. For instance, based on 3-node triangular elements, Arnold et al. used a cubic bubble function in each element to increase the displacement DOFs, known as the MINI element [26, 27]. It has been shown that this method belongs to the VMS framework [28], and its fulfillment of the inf-sup condition can be analytically evidenced using the two-level projection framework [7]. The Crouzeix-Raviart element [29] transfers the DOFs from the triangular vertices to edges, increasing the constraint ratio since, for triangular topology, the number of edges is greater than that of vertices. More details about FEM technology for divergence constraint issues can be found in Refs. [2, 4, 30].

In the past two decades, various novel approximations equipped with global smoothed shape functions, such as moving least-squares approximation [31], reproducing kernel approximation [32], radial basis functions [33, 34], maximum-entropy approximation [35], and NURBS approximation [36, 37], have been proposed. In these approaches, the approximant pressure evaluated by the derivatives of global continuous shape functions also maintains a constraint ratio of 2 in 2D incompressible elasticity problems. However, the corresponding results still show lower accuracy caused by locking [38, 39]. Widely-used locking-free technologies for FEM are introduced in these approaches to enhance their performance. For example, Moutsanidis et al. employed selective integration and B-bar, F-bar methods for reproducing kernel particle methods [40, 41]. Wang et al. applied selective integration schemes with bubble-stabilized functions to node-based smoothed particle FEM [42]. Elguedj et al. proposed the B-bar and F-bar NURBS formulations for linear and nonlinear incompressible elasticity. Chen et al. adopted the pressure projection approach for reproducing kernel formulations for nearly-incompressible problems [43], which was later extended to Stokes flow formulations by Goh et al. [44]. Bombarde et al. developed a block-wise NURBS formulation for shell structures, eliminating locking via pressure projection [45]. Most of these approximations offer better flexibility for arranging DOFs since their shape function constructions are no longer element-dependent. Huerta et al. proposed a reproducing kernel approximation with divergence-free basis functions to avoid volumetric strain entirely [46], although this approach is unsuitable for compressible cases. Wu et al. added extra displacement DOFs in FEM elements to resolve the locking issue, constructing local shape functions using generalized meshfree interpolation to maintain consistency [47]. Vu-Huu et al. employed different-order polygonal finite element shape functions to approximate displacement and pressure, embedding a bubble function in each element for stabilization.

This work proposes a more precise optimal divergence constraint ratio and implements a locking-free and stabilized mixed FEM-Meshfree formulation with this optimal constraint ratio. Firstly, the inf-sup condition is derived in a new form, showing that the inf-sup value equals the lowest non-zero eigenvalue of dilatation stiffness. Subsequently, involving a complete polynomial space with dimensions identical to DOFs, this inf-sup value can be bounded by a two-level estimator. This estimator provides a strong link between the inf-sup value and the pressure DOFs, making it possible to justify the locking status by counting the pressure nodes. From this estimator, two key ratios, namely the locking ratio and the stabilized ratio, are defined. If the constraint ratio exceeds the locking ratio, the formulation will show severe locking. If the constraint ratio is lower than the locking ratio but greater than the stabilized ratio, the displacement solution is free from locking, but the pressure shows oscillation, known as the spurious pressure mode, and the inf-sup condition is not satisfied. When the constraint ratio is lower than the stabilized ratio, the formulation achieves satisfactory results, and the inf-sup condition is fulfilled. The stabilized ratio is preferable to the locking ratio, but determining the stabilized ratio is not trivial. The locking ratio can be determined by the total DOFs of the entire system, but the stabilized ratio relates to the topology of the pressure. Currently, the stabilized ratio should be determined numerically. Consequently, these two constraint ratios are considered optimal, and you can choose the better one based on your requirements. If you focus only on the displacement result, the locking ratio is sufficient. If capturing the pressure behavior is the aim, the stabilized ratio should be used. For checking a formulation's locking status, these two optimal constraint ratios are more precise than rough constraint counting in a continuous sense and easier than the inf-sup test.

Furthermore, a mixed FEM-Meshfree formulation is proposed to verify the optimal constraint ratio. In this mixed formulation, the displacement is approximated by traditional finite element methods, and the pressure is discretized by reproducing kernel meshfree approximation. With the aid of global RK shape functions, the pressure's DOFs can be adjusted arbitrarily without considering approximation order and numerical integration issues. Accordingly, a bubble meshing scheme is proposed to generate a specific number of pressure nodes, maintaining the constraint ratio as optimal.

The remainder of this paper is organized as follows: Section 2 reviews the mixed-formulation framework for incompressible elasticity and heat diffusion problems. In Section 3, a novel estimator of the inf-sup value is developed, from which the optimal divergence constraint ratio is obtained. Section 4 introduces the mixed FEM-Meshfree formulation and its corresponding mesh generator. Section 5 verifies the proposed optimal divergence constraint ratio using a set of inf-sup tests and benchmark examples, studying error convergence and stability properties for the mixed FEM-Meshfree approximation. Finally, the conclusions are presented in Section 6.

2. Mixed–formulation

2.1. Nearly–incompressible elasticity

Consider a body $\Omega \in \mathbb{R}^{n_d}$ with boundary Γ in n_d-dimension, where the Γ_t and Γ_g denotes its natural boundary and essential boundary such that $\Gamma_t \cup \Gamma_g = \Gamma$, $\Gamma_t \cap \Gamma_g = \varnothing$. The corresponding governing equations for mixed-formulation are given by:

$$\begin{cases} \nabla \cdot \boldsymbol{\sigma} + \boldsymbol{b} = \boldsymbol{0} & \text{in } \Omega \\ \frac{p}{\kappa} + \nabla \cdot \boldsymbol{u} = 0 & \text{in } \Omega \\ \boldsymbol{\sigma} \cdot \boldsymbol{n} = \boldsymbol{t} & \text{on } \Gamma_t \\ \boldsymbol{u} = \boldsymbol{g} & \text{on } \Gamma_g \end{cases} \tag{2}$$

where $\boldsymbol{u}$ and p, stand for displacement and hydrostatic pressure respectively, are the variables of this problem. $\boldsymbol{\sigma}$ denotes to stress tensor and has the following form:

$$\boldsymbol{\sigma}(\boldsymbol{u}, p) = p\mathbf{1} + 2\mu \nabla^d \boldsymbol{u} \tag{3}$$

in which $\mathbf{1} = \delta_{ij} \boldsymbol{e}_i \otimes \boldsymbol{e}_j$ is second order identity tensor. $\nabla^d \cdot \boldsymbol{u}$ is the deviatoric gradient of $\boldsymbol{u}$ and can be evaluated by:

$$\nabla^d \boldsymbol{u} = \frac{1}{2}(\boldsymbol{u}\nabla + \nabla \boldsymbol{u}) - \frac{1}{3} \nabla \cdot \boldsymbol{u} \tag{4}$$

and κ, μ are the bulk modulus and shear modulus, and they can be represented by Young's modulus E and Poisson's ratio ν:

$$\kappa = \frac{E}{2(1-2\nu)}, \quad \mu = \frac{E}{2(1+\nu)} \tag{5}$$

Moreover, $\boldsymbol{b}$ denotes to prescribed body force in Ω. $\boldsymbol{t}$, $\boldsymbol{g}$ are prescribed traction and displacement on natural and essential boundaries respectively.

In accordance with Galerkin formulation, the weak form can be given by: Find $\boldsymbol{u} \in V$, $p \in Q$,

$$\begin{cases} a(\boldsymbol{v}, \boldsymbol{u}) + b(\boldsymbol{v}, p) = f(\boldsymbol{v}) & \forall \boldsymbol{v} \in V \\ b(\boldsymbol{u}, q) + c(q, p) = 0 & \forall q \in Q \end{cases} \tag{6}$$

with the spaces V, Q defined by:

$$V = \{\boldsymbol{v} \in H^1(\Omega)^2 \mid \boldsymbol{v} = \boldsymbol{g}, \text{ on } \Gamma_g\} \tag{7}$$

$$Q = \{q \in L^2(\Omega) | \int_\Omega q d\Omega = 0\} \tag{8}$$

where $a : V \times V \to \mathbb{R}$, $b : V \times Q \to \mathbb{R}$ and $c : Q \times Q \to \mathbb{R}$ are bilinear forms, and $f : V \to \mathbb{R}$ is the linear form. In elasticity problem, they has the following forms:

$$a(\boldsymbol{v}, \boldsymbol{u}) = \int_\Omega \nabla^d \boldsymbol{v} : \nabla^d \boldsymbol{u} d\Omega \tag{9}$$

$$b(\boldsymbol{v}, q) = \int_\Omega \nabla \cdot \boldsymbol{v} q d\Omega \tag{10}$$

$$c(q, p) = -\int_\Omega \frac{1}{3\kappa} q p d\Omega \tag{11}$$

$$f(\boldsymbol{v}) = \int_{\Gamma_t} \boldsymbol{v} \cdot \boldsymbol{t} d\Gamma + \int_\Omega \boldsymbol{v} \cdot \boldsymbol{b} d\Omega \tag{12}$$

2.2. Ritz–Galerkin problem and volumetric locking

In mixed–formulation framework, the displacement and pressure can be discretized by different approximations. The approximant displacement $\boldsymbol{u}_h$ and approximant pressure p_h can be expressed by:

$$\boldsymbol{u}_h(\boldsymbol{x}) = \sum_{I=1}^{n_u} N_I(\boldsymbol{x}) \boldsymbol{u}_I, \quad p_h(\boldsymbol{x}) = \sum_{K=1}^{n_p} \Psi_K(\boldsymbol{x}) p_K \tag{13}$$

leading these approximations into the weak form of Eq. (6) yields the following Ritz–Galerkin problems: Find $\boldsymbol{u}_h \in V_h,\ p_h \in Q_h$,

$$\begin{cases} a(\boldsymbol{v}_h, \boldsymbol{u}_h) + b(\boldsymbol{v}_h, p_h) = f(\boldsymbol{v}_h) & \forall \boldsymbol{v}_h \in V_h \\ b(\boldsymbol{u}_h, q_h) + c(q_h, p_h) = 0 & \forall q_h \in Q_h \end{cases} \tag{14}$$

For nearly incompressible material, the Poisson ratio approaches to 0.5, the bulking modulus κ will turns to be infinity based on Eq. (5). Then the bilinear form c in Eq. (11) turns to be zero. And the weak form of Eq. (14) belong to an enforcement of the volumetric strain $\nabla \cdot \boldsymbol{u}_h$ to be zero using the Lagrangian multiplier method, where p_h is the Lagrangian multiplier.

Furthermore, from the second line of Eq. (14), we have:

$$b(\boldsymbol{u}_h, q_h) + c(q_h, p_h) = (q_h, \nabla \cdot \boldsymbol{u}_h) - (q_h, \frac{1}{3\kappa} p_h) = 0, \quad \forall q_h \in Q_h \tag{15}$$

or

$$(q_h, 3\kappa \nabla \cdot \boldsymbol{u}_h) = (q_h, p_h) = (q_h, \tilde{\nabla} \cdot \boldsymbol{u}_h), \quad \forall q_h \in Q_h \tag{16}$$

where $(\bullet, \bullet)$ is the inner product operator evaluated by:

$$(q, p) := \int_\Omega q p d\Omega \tag{17}$$

Obviously in Eq. (16), p_h is the orthogonal projection of $3\kappa\nabla\cdot\boldsymbol{u}_h$ regarded to the space Q_h [1], and, for further development, use upper tilde to name the projection operator, i.e. $p_h = \tilde{\nabla}\cdot\boldsymbol{u}_h$.

$$\begin{aligned} b(\boldsymbol{v}_h, p_h) &= (\underbrace{\nabla\cdot\boldsymbol{v}_h - \tilde{\nabla}\cdot\boldsymbol{v}_h, p_h}_{0}) + (\tilde{\nabla}\cdot\boldsymbol{v}_h, \underbrace{p_h}_{3\kappa\tilde{\nabla}\cdot\boldsymbol{u}_h}) \\ &= (\tilde{\nabla}\cdot\boldsymbol{v}_h, 3\kappa\tilde{\nabla}\cdot\boldsymbol{u}_h) \\ &= \tilde{a}(\boldsymbol{v}_h, \boldsymbol{u}_h) \end{aligned} \tag{18}$$

where the bilinear form $\tilde{a} : V_h \times V_h \to \mathbb{R}$ is defined by:

$$\tilde{a}(\boldsymbol{v}_h, \boldsymbol{u}_h) = \int_\Omega 3\kappa\tilde{\nabla}\cdot\boldsymbol{v}_h\tilde{\nabla}\cdot\boldsymbol{u}_h d\Omega \tag{19}$$

Accordingly, the problem of Eq. (14) becomes to be one variable form: Find $\boldsymbol{u}_h \in V_h$,

$$a(\boldsymbol{v}_h, \boldsymbol{u}_h) + \tilde{a}(\boldsymbol{v}_h, \boldsymbol{u}_h) = f(\boldsymbol{v}_h), \quad \forall\boldsymbol{v}_h \in V_h \tag{20}$$

As $\kappa \to \infty$, Eq. (20)can be regarded as an enforcement of volumetric strain using penalty method, where $\tilde{a}$ is the penalty term. However, it should be noted that, if the mixed–formulation wants to get a satisfactory result, this orthogonal projection must be surjective[48]. If this projection is not surjective, for a given $p_h \in Q_h$ it possibly cannot find a $\boldsymbol{u}_h \in V_h$ such that $p_h = 3\kappa\nabla\cdot\boldsymbol{u}_h$. It will lead to a much smaller displacement than expected, and an oscillated pressure result. This phenomenon is so–call volumetric locking.

3. Optimal volumetric constraint ratio

3.1. Inf–sup condition and its eigenvalue problem

To ensure surjectivity of othogonal projection and the result's accuracy, the approximations of Eq.(7) should satisfy the inf-sup condition, also known as the Ladyzhenskaya–Babuška–Brezzi condition [4]:

$$\inf_{q_h\in Q_h}\sup_{\boldsymbol{v}_h\in V_h}\frac{|b(q_h, \boldsymbol{v}_h)|}{\|q_h\|_Q\|\boldsymbol{v}_h\|_V} \geq \beta > 0 \tag{21}$$

in which β, namely inf-sup value, is a constant independent of characterized element size h. The norms of $\|\bullet\|_V$ and $\|\bullet\|_Q$ can be flexibly defined by:

$$\|\boldsymbol{v}\|_V^2 = \int_\Omega \nabla^s\boldsymbol{v} : \nabla^s\boldsymbol{v} d\Omega \tag{22}$$

$$\|q\|_Q^2 = \int_\Omega \frac{1}{3\kappa}q^2 d\Omega \tag{23}$$

Lemma 1. *Suppose $\mathcal{P}_h : V_h \to Q_h$ is the orthogonal projection operator of divergence operator $\mathcal{P} := 3\kappa\nabla\cdot$, i.e. $\mathcal{P}_h := 3\kappa\tilde{\nabla}\cdot$ and satisfied Eq.* (16)*. Such that the inf-sup value can be estimated by:*

$$\beta \leq \inf_{V_h' \subset V_h \setminus \ker \mathcal{P}_h} \sup_{v_h \in V_h'} \frac{\|\mathcal{P}_h \boldsymbol{v}_h\|_Q}{\|\boldsymbol{v}_h\|_V} \tag{24}$$

in which $\ker \mathcal{P}_h \subset V$ *is the kernel of* $\mathcal{P}_h$ *defined by* $\ker \mathcal{P}_h := \{\boldsymbol{v} \in V \mid \mathcal{P}_h \boldsymbol{v} = 0\}$.

Proof. As the definition of $\mathcal{P}_h$, $\mathrm{Im}\mathcal{P}_h \in Q_h$, the Eq. (21) can be rewritten as:

$$\begin{aligned}\beta &\leq \inf_{q_h \in Q_h} \sup_{\boldsymbol{v}_h \in V_h} \frac{|b(q_h, \boldsymbol{v}_h)|}{\|q_h\|_Q \|\boldsymbol{v}_h\|_V} = \inf_{q_h \in Q_h} \sup_{\boldsymbol{v}_h \in V_h} \frac{|(q_h, \frac{1}{3\kappa}\mathcal{P}\boldsymbol{v}_h)|}{\|q_h\|_Q \|\boldsymbol{v}_h\|_V} \\ &\leq \inf_{q_h \in \mathrm{Im}\mathcal{P}_h} \sup_{\boldsymbol{v}_h \in V_h} \frac{|\frac{1}{3\kappa}(q_h, \mathcal{P}_h \boldsymbol{v}_h)|}{\|q_h\|_Q \|\boldsymbol{v}_h\|_V}\end{aligned} \tag{25}$$

For a given $q_h \in \mathrm{Im}\mathcal{P}_h$, suppose a space $V_h' \subseteq V_h \setminus \ker P_h$ defined by:

$$V_h' = \{\boldsymbol{v}_h \in V_h \mid \mathcal{P}_h \boldsymbol{v}_h = q_h\} \tag{26}$$

Since $\mathrm{Im}\mathcal{P}_h \in Q_h$, in accordance with Cauchy-Schwarz inequality, we have:

$$\left|\frac{1}{3\kappa}(q_h, \mathcal{P}_h \boldsymbol{v}_h)\right| \leq \|q_h\|_Q \|\mathcal{P}_h \boldsymbol{v}_h\|_Q \tag{27}$$

where this equality is holding if and only if $q_h = \mathcal{P}_h \boldsymbol{v}_h$, i.e.,

$$\left|\frac{1}{3\kappa}(q_h, \mathcal{P}_h \boldsymbol{v}_h)\right| = \|q_h\|_Q \|\mathcal{P}_h \boldsymbol{v}_h\|_Q, \quad \forall \boldsymbol{v}_h \in V_h' \tag{28}$$

And the following relationship can be evidenced:

$$\sup_{\boldsymbol{v}_h \in V_h} \frac{\left|\frac{1}{3\kappa}(q_h, \mathcal{P}_h \boldsymbol{v}_h)\right|}{\|q_h\|_Q \|\boldsymbol{v}_h\|_V} = \sup_{\boldsymbol{v}_h \in V_h'} \frac{\|\mathcal{P}_h \boldsymbol{v}_h\|_Q}{\|\boldsymbol{v}_h\|_V}, \quad \forall q_h \in \mathrm{Im}\mathcal{P}_h \tag{29}$$

Consequently, with a combination of Eqs. (25) and (29), Eq. (24) can be obtained.

Remark 1. *With Lemma 1 and the norm definitions in Eqs.* (22),(23)*, the square of inf–sup value can further bounded by:*

$$\beta^2 \leq \inf_{V_h' \subset V_h \setminus \ker \mathcal{P}_h} \sup_{v_h \in V_h'} \frac{\|\mathcal{P}_h \boldsymbol{v}_h\|_Q^2}{\|\boldsymbol{v}_h\|_V^2} = \inf_{V_h' \subset V_h \setminus \ker \mathcal{P}_h} \sup_{v_h \in V_h'} \frac{\tilde{a}(\boldsymbol{v}_h, \boldsymbol{v}_h)}{a(\boldsymbol{v}_h, \boldsymbol{v}_h)} \tag{30}$$

The left hand side of above equation is consistance with the minimum-maximum principle [49] and again proof the equivalence with traditional numerical inf-sup test [5]. Since that, β^2 evaluates the non-zero general eigenvalue of $\tilde{a}$ and a in Eq. (20)*.*

3.2. Inf–sup value estimator

Theorem 1. *Suppose that P_{n_u} is a polynomial space with n_u dimensions, and V_{n_u} is the polynomial displacement space, $V_{n_u} = P_{n_u}^{n_d}$. The optimal dofs of pressure n_p is equal to $n_c = \dim(V_{n_c} \setminus \ker \mathcal{P})$.*

$$\beta \leq \beta_s + Ch \tag{31}$$

with

$$\beta_s = \inf_{V' \subset V_{n_u} \setminus \ker \mathcal{P}_h \mathcal{I}_h} \sup_{v \in V'} \frac{\|\mathcal{P}\boldsymbol{v}\|_Q}{\|\boldsymbol{v}\|_V} \tag{32}$$

Proof. As the dimensions of V_h and V_{n_u} is identical, $\dim V_{n_u} = \dim V_h = n_d \times n_u$. There exists a unique $\boldsymbol{v} \in V_{n_u}$ satisfing $\boldsymbol{v}_h = \mathcal{I}_h \boldsymbol{v}$. And the right side of Eq. (24) becomes:

$$\inf_{V_h' \subset V_h \setminus \ker \mathcal{P}_h} \sup_{\boldsymbol{v}_h \in V_h'} \frac{\|\mathcal{P}_h \boldsymbol{v}_h\|_Q}{\|\boldsymbol{v}_h\|_V} = \inf_{V' \subset V_{n_u} \setminus \ker \mathcal{P}_h \mathcal{I}_h} \sup_{\boldsymbol{v} \in V'} \frac{\|\mathcal{P}_h \mathcal{I}_h \boldsymbol{v}\|_Q}{\|\mathcal{I}_h \boldsymbol{v}\|_V} \tag{33}$$

In accordance with triangular inequality, Cauchy-Schwarz inequality and the relationship of Eqs. (**??**), we have:

$$\begin{aligned} \|\mathcal{P}_h \mathcal{I}_h \boldsymbol{v}\|_Q &= \sup_{q_h \in Q_h} \frac{\left|\frac{1}{3\kappa}(q_h, \mathcal{P}_h \mathcal{I}_h \boldsymbol{v})\right|}{\|q_h\|_Q} = \sup_{q_h \in Q_h} \frac{|(q_h, \mathcal{P}\mathcal{I}_h \boldsymbol{v})|}{\|q_h\|_Q} \\ &\leq \sup_{q_h \in Q_h} \frac{|(q_h, \mathcal{P}\boldsymbol{v})| + |(q_h, \mathcal{P}\boldsymbol{v} - \mathcal{P}\mathcal{I}_h \boldsymbol{v})|}{\|q_h\|_Q} \\ &\leq \|\mathcal{P}\boldsymbol{v}\|_Q + \|\mathcal{P}(\mathcal{I} - \mathcal{I}_h)\boldsymbol{v}\|_Q \end{aligned} \tag{34}$$

Obviously, the second and third terms on the right side of Eq. (34) are the interpolation error and the orthogonal projection error for approximations in V_h, and can be evaluated by [50]:

$$\|\mathcal{P}(\mathcal{I} - \mathcal{I}_h)\boldsymbol{v}\|_Q \leq Ch\|\boldsymbol{v}\|_V \tag{35}$$

It can be obtained that $\|\mathcal{I}_h \boldsymbol{v}\|_V \geq C\|\boldsymbol{v}\|_V$ from close graph theorem [28]. And considering it with Eqs. (34)-(35), the right side of Eq. (33) can be represented as:

$$\inf_{V' \subset V_{n_u} \setminus \ker \mathcal{P}_h \mathcal{I}_h} \sup_{\boldsymbol{v} \in V'} \frac{\|\mathcal{P}_h \mathcal{I}_h \boldsymbol{v}\|_Q}{\|\mathcal{I}_h \boldsymbol{v}\|_V} \leq \inf_{V' \subset V_{n_u} \setminus \ker \mathcal{P}_h \mathcal{I}_h} \sup_{\boldsymbol{v} \in V'} \frac{\|\mathcal{P}\boldsymbol{v}\|_Q}{\|\boldsymbol{v}\|_V} + Ch \tag{36}$$

Substituting Eqs. (33),(36) into (24) can get the following relationship of Eqs. (31), (32).

As we can see in Eqs. (31) and (32), $\beta_s \geq 0$, whether the β_s equal to 0 or not determines if the formulation satisfies the inf–sup condition or not. If $\beta_s > 0$, as the mesh refining, the second term in the right-hand side of Eq. (31) can be ignored. In contrast, if $\beta_s = 0$, the second term will dominate, and the inf-sup condition will not be satisfied, leading to numerical instability.

3.3. Polynomial–wise constraint counting

From the above subsection, we can know that whether the β_s is zero or not determines whether the mixed–formulation can fulfill the inf–sup condition. According to the expression of $beta_s$ in Eq. (32), as $\beta_s = 0$, the variable $\boldsymbol{v}$ should belong to $\ker \mathcal{P}$, so the dimensions of the subspace in which $\beta_s \neq 0$, namely n_s, can be evaluated by:

$$n_s = \dim(V_{n_s} \setminus \ker \mathcal{P}) \tag{37}$$

To further construction of the relationship between inf–sup value estimator in Eq. (31) and constraint ratio $r = \frac{n_d \times n_u}{n_p}$, we should find the displacement and pressure DOFs in Eq. (31). With the definition of V_{n_u}, the number of displacement DOFs is easy to be evaluated by:

$$n_u = \dim V_{n_u} \tag{38}$$

With well-pose nodal distributions of displacement and pressure, the number of pressure DOFs has the following relationship:

$$n_p = \dim Q_h = \dim(\mathrm{Im}\mathcal{P}_h) = \dim(V_{n_u} \setminus \ker \mathcal{P}_h \mathcal{I}_h) \tag{39}$$

Fig. 1 illustrates how the relationship between n_s, n_p and n_u influence the fulfillment of inf–sup conditon:

- As $n_p > n_s$, there must exist a subspace in space $V_{n_u} \setminus \ker \mathcal{P}_h \mathcal{I}_h$ belong to $\ker \mathcal{P}$, resulting $\beta_s = 0$, i.e. $V_{n_u} \setminus \ker \mathcal{P}_h \mathcal{I}_h \cap \ker \mathcal{P} \neq \varnothing$. At this circumstance, the inf–sup condition cannot be satisfied and the formulation will suffer from volumetric locking.

- As $n_p \leq n_s$, for a well–pose nodal distributions, the space $\boldsymbol{V}_{n_u} \setminus \ker \mathcal{P}_h \mathcal{I}_h$ may be a subset of $V_{n_u} \setminus \ker \mathcal{P}$. Then, the β_s will remain to be nonzero, and the formulation will be locking–free.

Summarily, the formulation can satisfy the inf–sup condition and alleviates the volumetric locking at least the number of pressure nodes n_p should be less than n_s, so we name n_s as stabilized number of pressure nodes. At this moment, the volumetric constraint ratio should meet the following relation to ensure inf–sup conditon:

$$r_{opt} \geq \frac{n_d \times n_u}{n_s} \tag{40}$$

Remark 2. *Some uniform element with special arrangement, like union–jack element arrangement for 3–node triangular element, can pass the inf–sup test[6], but its pressure DOFs number is greater than n_s. This is caused by that, the union–jack arrangement leads to lower the nonzero eigenvalue number of $\tilde{a}$ and a in Eq. (20), and the corresponding nonzero eigenvalue number is less than stabilized number n_s, satisfing Eq. (40). The similar cases about this special element arrangement is too few, so it is more straightforword to use the number of pressure nodes n_p to measure $\dim(V_{n_u} \setminus \ker \mathcal{P}_h \mathcal{I}_h)$.*

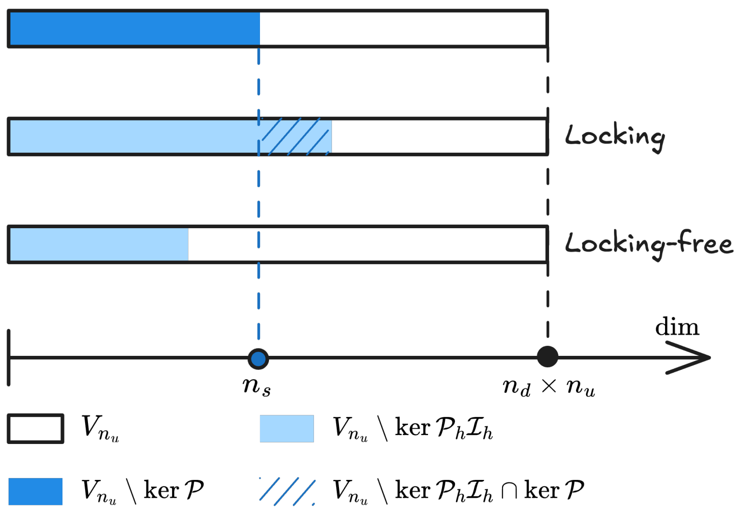

Figure 1: Illustration of estimator

Remark 3. *It is obviously that the traditional optimal constraint ratio can not fulfill this condition. However, not all formulations satisfing this condition can totally avoid volumetric locking. It is because that $n_p \leq n_s$ is not equivalent with $V_{n_u} \setminus \ker \mathcal{P}_h \mathcal{I}_h \subset V_{n_u} \setminus \ker \mathcal{P}$. Fortunately, the well–pose nodal distributions of displacement and pressure can ensure this that will be shown in the subsequent sections.*

3.4. Optimal volumetric constraint ratio

The fulfillment of inf–sup conditon should require the number of pressure nodes n_p lower than the stabilized number n_s, and now, we will demonstrate how to determine n_s for a specific number of displacement DOFs.

In 2D case, for instance, we first consider the linear polynomial displacement space V_3 is given by:

$$V_3 = \text{span}\left\{ \begin{pmatrix}1\\0\end{pmatrix}, \begin{pmatrix}0\\1\end{pmatrix}, \begin{pmatrix}x\\0\end{pmatrix}, \begin{pmatrix}0\\x\end{pmatrix}, \begin{pmatrix}y\\0\end{pmatrix}, \begin{pmatrix}0\\y\end{pmatrix} \right\} \tag{41}$$

or rearranged as follows,

$$V_3 = \text{span}\left\{ \underbrace{\begin{pmatrix}1\\0\end{pmatrix}, \begin{pmatrix}0\\1\end{pmatrix}, \begin{pmatrix}y\\0\end{pmatrix}, \begin{pmatrix}0\\x\end{pmatrix}, \begin{pmatrix}x\\-y\end{pmatrix}}_{\ker \mathcal{P}}, \underbrace{\begin{pmatrix}x\\y\end{pmatrix}}_{V_3 \setminus \ker \mathcal{P}} \right\} \tag{42}$$

It can be counted that, for $n_u = 3$, $n_s = 1$. Following the path, the displacement space with quadratic polynomial base namely V_6 can be stated as:

$$V_6 = \text{span}\left\{ \begin{gathered} \overbrace{\begin{pmatrix}1\\0\end{pmatrix}, \begin{pmatrix}0\\1\end{pmatrix}, \begin{pmatrix}y\\0\end{pmatrix}, \begin{pmatrix}0\\x\end{pmatrix}, \begin{pmatrix}x\\-y\end{pmatrix}, \begin{pmatrix}x^2\\-2xy\end{pmatrix}, \begin{pmatrix}y^2\\0\end{pmatrix}, \begin{pmatrix}0\\x^2\end{pmatrix}, \begin{pmatrix}-2xy\\y^2\end{pmatrix}}^{\ker \mathcal{P}}, \\ \underbrace{\begin{pmatrix}x\\y\end{pmatrix}, \begin{pmatrix}x^2\\2xy\end{pmatrix}, \begin{pmatrix}2xy\\y^2\end{pmatrix}}_{V_6 \backslash \ker \mathcal{P}} \end{gathered} \right\} \tag{43}$$

In this circumstance, $n_s = 3$. As the order of polynomial space increasing, the every optimal numbers of constraint dofs for each order are listed in Table. 1, in which n denoted by the order of space P_{n_u}. For the flexibility of usage, the relation between n_u and n_c is summarized as follows:

$$n_s = \frac{n(n+1)}{2}, \quad n = \left\lfloor \frac{\sqrt{1+8n_u} - 3}{2} \right\rfloor \tag{44}$$

Table 1: Relationship between displacement DOFs and stabilized number

	2D		3D	
n	n_u	n_s	n_u	n_s
1	3	1	4	1
2	6	3	10	4
3	10	6	20	10
4	15	10	35	20
$\vdots$	$\vdots$	$\vdots$	$\vdots$	$\vdots$

For 3D case, following the path in 2D, the lienar polynomial space V_4 is considered herein, and the arranged space of V_4 is listed as follows:

$$V_4 = \text{span}\left\{ \begin{gathered} \overbrace{\begin{pmatrix}1\\0\\0\end{pmatrix}, \begin{pmatrix}0\\1\\0\end{pmatrix}, \begin{pmatrix}0\\0\\1\end{pmatrix}, \begin{pmatrix}0\\x\\0\end{pmatrix}, \begin{pmatrix}0\\0\\x\end{pmatrix}, \begin{pmatrix}y\\0\\0\end{pmatrix}}^{\ker \mathcal{P}}, \\ \underbrace{\begin{pmatrix}0\\0\\y\end{pmatrix}, \begin{pmatrix}z\\0\\0\end{pmatrix}, \begin{pmatrix}0\\z\\0\end{pmatrix}, \begin{pmatrix}x\\-y\\0\end{pmatrix}, \begin{pmatrix}x\\0\\-z\end{pmatrix}}_{\ker \mathcal{P}}, \underbrace{\begin{pmatrix}x\\y\\z\end{pmatrix}}_{V_{n_u} \backslash \ker \mathcal{P}} \end{gathered} \right\} \tag{45}$$

For brevity, the stabilized numbers for higher order polynomial displacement space is directly listed in Table. 1, and it can be summarized that, for a given number of displacement DOFs, the stabilized number for pressure DOFs can be calculated as follows:

$$n_s = \frac{n(n+1)(n+2)}{6} \tag{46}$$

$$n = \left\lfloor \left(3n_u + \frac{1}{3}\sqrt{81n_u^2 - \frac{1}{3}}\right)^{\frac{1}{3}} + \frac{1}{3\left(3n_u + \frac{1}{3}\sqrt{81n_u^2 - \frac{1}{3}}\right)^{\frac{1}{3}}} - 2 \right\rfloor \tag{47}$$

4. FE–Meshfree mixed formulation with optimal constraint

In the proposed mixed-formulation, the displacement is approximated using three-node, six-node triangular elements and four-node, eight-node quadrilateral elements [2]. In order to flexcially adjust to let the dofs of pressure meets to be optimal, the reproducing kernel meshfree approximation is involved to approximate pressure.

4.1. Reproducing kernel meshfree approximation

In accordance with the reproducing kernel approximation, the entire domain Ω is discretized by n_p meshfree points, $\{\boldsymbol{x}_I\}_{I=1}^{n_p}$. Each meshfree point equips a meshfree shape function Ψ_I and nodal coefficient p_I, and the approximated pressure namely p_h can be presented by:

$$p_h(\boldsymbol{x}) = \sum_{I=1}^{n_p} \Psi_I(\boldsymbol{x}) p_I \tag{48}$$

where, in the reproducing kernel approximation framework, the shape function Ψ_I is given by:

$$\Psi_I(\boldsymbol{x}) = \boldsymbol{c}(\boldsymbol{x}_I - \boldsymbol{x})\boldsymbol{p}(\boldsymbol{x}_I - \boldsymbol{x})\phi(\boldsymbol{x}_I - \boldsymbol{x}) \tag{49}$$

in which $\boldsymbol{p}$ is the basis function, especially for 2D quadratic basis function, having the following form:

$$\boldsymbol{p}(\boldsymbol{x}) = \{1, x, y, x^2, xy, y^2\}^T \tag{50}$$

and ϕ stands for the kernel function. In this work, the traditional Cubic B-spline function with square suppot is used as the kernel function:

$$\phi(\boldsymbol{x}_I - \boldsymbol{x}) = \phi(s_x)\phi(s_y), \quad s_i = \frac{\|\boldsymbol{x}_I - \boldsymbol{x}\|}{\bar{s}_{iI}} \tag{51}$$

with

$$\phi(s) = \frac{1}{3!}\begin{cases} (2-2s)^3 - 4(1-2s)^3 & s \leq \frac{1}{2} \\ (2-2s)^3 & \frac{1}{2} < s < 1 \\ 0 & s > 1 \end{cases} \tag{52}$$

where $\bar{s}_{iI}$'s are the support size towards the i-direction for the shape function Ψ_I. The correction function $\boldsymbol{c}$ can be determined by the following so-call consistency condition:

$$\sum_{I=1}^{n_p} \Psi_I(\boldsymbol{x})\boldsymbol{p}(\boldsymbol{x}_I) = \boldsymbol{p}(\boldsymbol{x}) \tag{53}$$

or equivalent shifted form:

$$\sum_{I=1}^{n_p} \Psi_I(\boldsymbol{x})\boldsymbol{p}(\boldsymbol{x}_I - \boldsymbol{x}) = \boldsymbol{p}(\boldsymbol{0}) \tag{54}$$

Substituting Eq. 49 into Eq. (54) leads to:

$$\boldsymbol{c}(\boldsymbol{x}_I - \boldsymbol{x}) = \boldsymbol{A}^{-1}(\boldsymbol{x}_I - \boldsymbol{x})\boldsymbol{p}(\boldsymbol{0}) \tag{55}$$

in which $\boldsymbol{A}$ is namely moment matrix evaluating by:

$$\boldsymbol{A}(\boldsymbol{x}_I - \boldsymbol{x}) = \sum_{I=1}^{n_p} \boldsymbol{p}(\boldsymbol{x}_I - \boldsymbol{x})\boldsymbol{p}^T(\boldsymbol{x}_I - \boldsymbol{x})\phi(\boldsymbol{x}_I - \boldsymbol{x}) \tag{56}$$

Taking Eq. (55) back to Eq. (49), the final form of reproducing kernel shape function can be got as:

$$\Psi_I(\boldsymbol{x}) = \boldsymbol{p}^T(\boldsymbol{0})\boldsymbol{A}^{-1}(\boldsymbol{x}_I - \boldsymbol{x})\phi(\boldsymbol{x}_I - \boldsymbol{x}) \tag{57}$$

4.2. Optimal pressure nodes distributions

In this subsection, the FE-meshfree mixed formulation is empolyed in inf–sup test [6] to validate the proposed estimator of inf–sup value. Consider the square domain $\Omega = (0,1) \otimes (0,1)$ in Fig. 2, the displacement is discretized by linear Triangular element (Tri3), Quadrilateral element (Quad4) with 4×4, 8×8, 16×16 and 32×32 elements, quadratic Triangular element (Tri6), Quadrilateral element (Quad8) with 2×2, 4×4, 8×8 and 16×16 elements, respectively. In order to avoid the influence of interpolation error, the uniform nodal distributions are used for pressure discretizations.

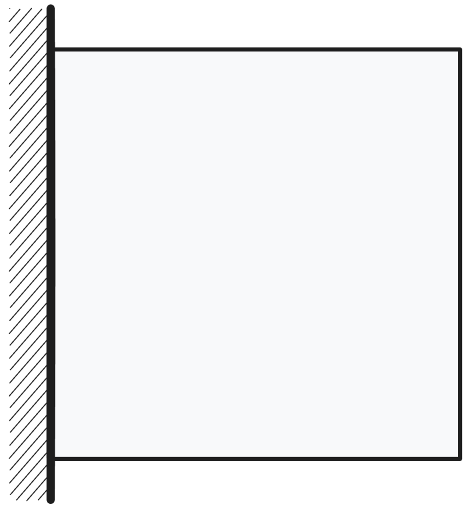

Figure 2: Illustration of inf–sup test

Figure 3 shows the corresponding results, in which the red line stands for the value of β respected to the number of pressure nodes n_p, the vertical dash line denotes to the stabilized number n_s. The deeper color of lines means the mesh refining. The results show that, no matter linear or quadratic elements, as n_p increases over the n_s, the *beta*'s value sharply decrease, and then the inf–sup condition cannot be maintained. This result is consistent with the discussion in Section 3, and again verify the effect of the proposed estimator.

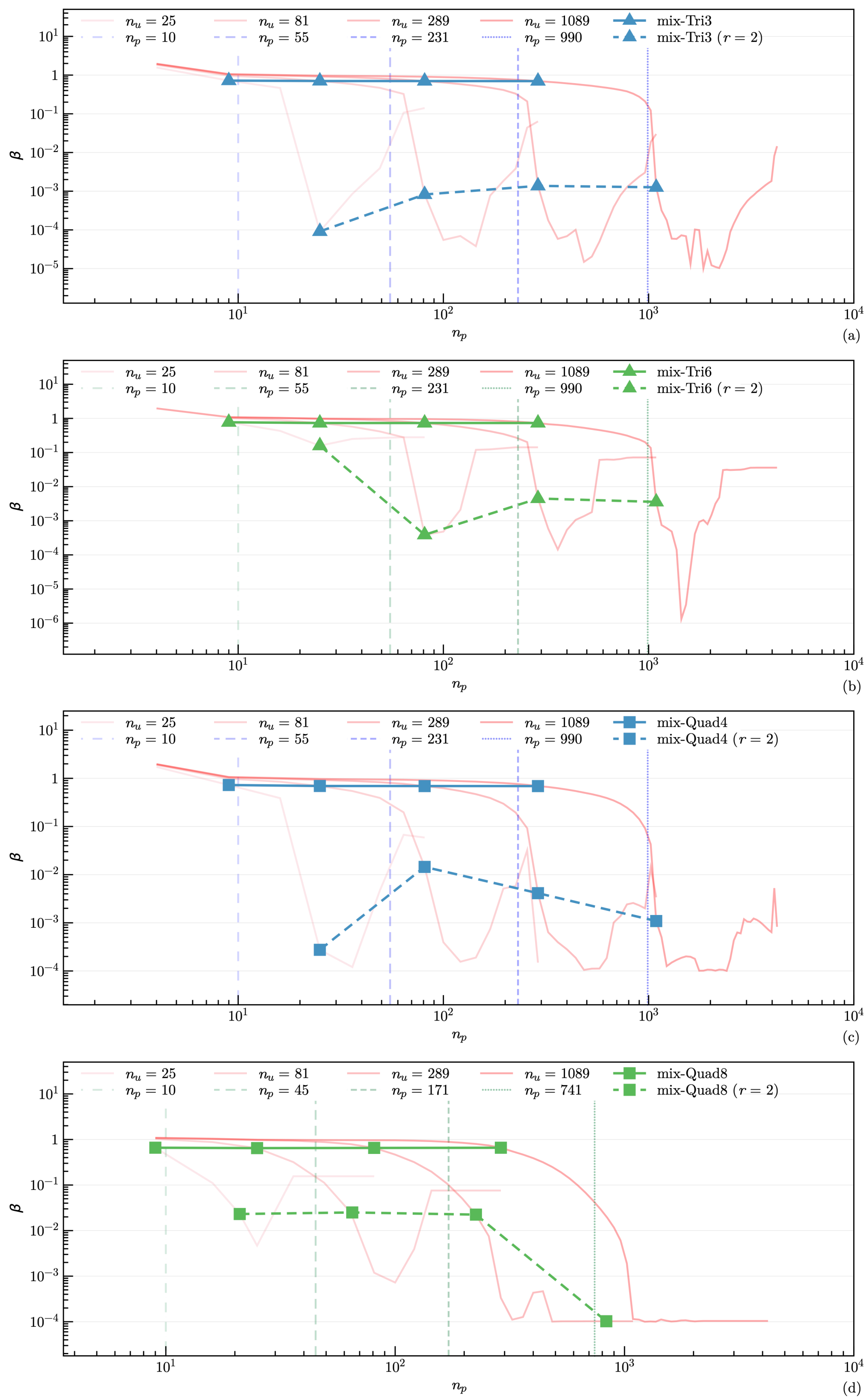

Figure 3: Inf–sup test for various finite element formulations:
(a) mix-Tri3; (b) mix-Tri6; (c) mix-Quad4; (d) mix-Quad8

Moreover, the mixed formulation's results with traditional optimal constraint ratio $r = n_d$ are listed in 3 as well, and the *beta* in this circumstance is already much smaller than those in optimal range. Considering the results shown above, the easy-programming and efficiency, the pressure nodes are chosen among the displacement nodes. The final schemes for linear and quadratic, 2D and 3D elements discretizations are shown in Figure 4, in which all constraint ratios are belong to the range of optimal ratio. The corresponding inf–sup test results for these schemes also be marked in Figure 2 and show that, with the mesh refining, their *beta*'s are always maintained in a non–negligible level.

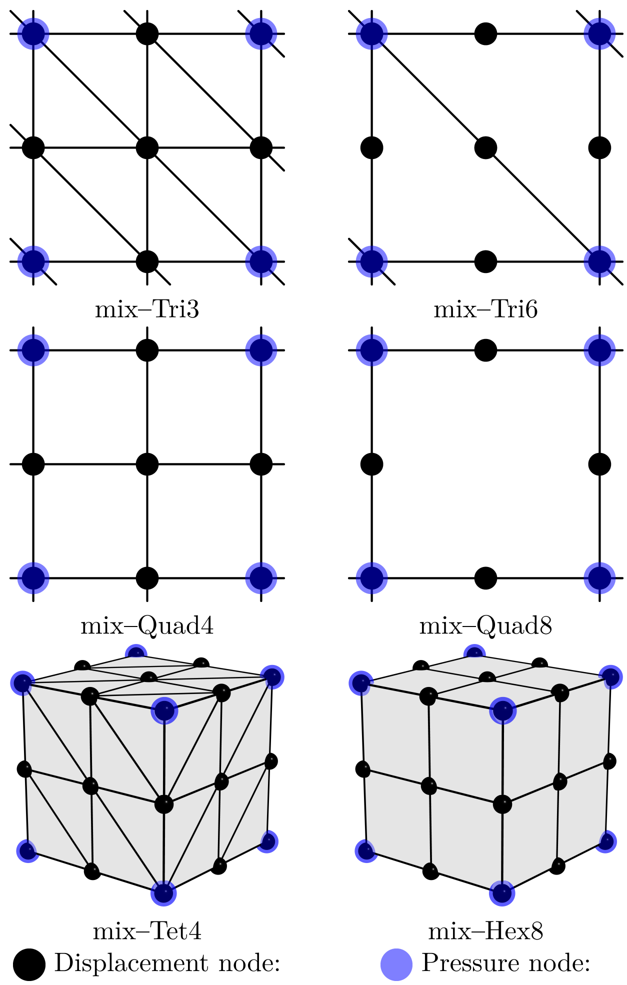

Figure 4: Nodal distribution schemes for FE-MF mixed formulations with $r = r_{opt}$

5. Numerical examples

5.1. Cantilever beam problem

Consider the cantilever beam problem shown in Figure 5 with length $L = 48$, width $D = 12$, and the incompressible material parameters are employed with Young's modulus $E = 3 \times 10^6$, Poisson's ratio $\nu = 0.5 - 10^{-8}$. The left hand side is fixed and the right side subject a concentrate force $P = 1000$. All the prescribed values in boundary conditions are evaluated by analytical solution that is given as follows[51]:

$$\begin{cases} u_x(\boldsymbol{x}) = -\dfrac{Py}{6\bar{E}I}\left((6L-3x)x + (2+\bar{\nu})(y^2 - \dfrac{D^2}{4})\right) \\ u_y(\boldsymbol{x}) = \dfrac{Py}{6\bar{E}I}\left(3\bar{\nu}y^2(L-x) + (4+5\bar{\nu})\dfrac{D^2 x}{4} + (3L-x)x^2\right) \end{cases} \tag{58}$$

where I is the beam's moment of inertia, $\bar{E}$ and $\bar{\nu}$ are the material parameters for plane strain hypothesis, they can be expressed by:

$$I = \frac{D^3}{12}, \quad \bar{E} = \frac{E}{1-\nu^2}, \quad \bar{\nu} = \frac{\nu}{1-\nu} \tag{59}$$

And correspondingly, the stress components are evaluated by

$$\begin{cases} \sigma_{xx} = -\dfrac{P(L-x)y}{I} \\ \sigma_{yy} = 0 \\ \sigma_{xy} = \dfrac{P}{2I}(\dfrac{D^2}{4} - y^2) \end{cases} \tag{60}$$

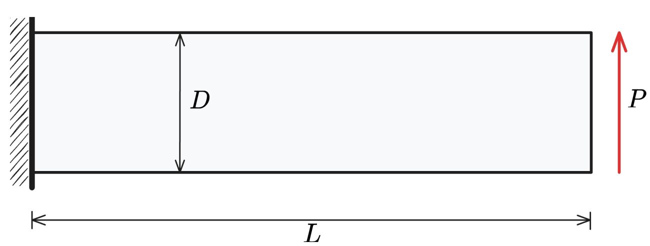

Figure 5: Illustration of cantilever beam problem

In this problem, the Quad4 element with 16×4, 32×8, 64×16, 128×32 grids, and Quad8 element with 8×2, 16×4, 32×8, 64×16 grids are employed for displacement discretization. The pressure are discretized by linear and quadratic meshfree approximations with 1.5 and 2.5 characterized support sizes respectively. The strain and pressure errors respected to pressure nodes n_p are displayed in Figure 6, where the vertical dashed lines stand for the stabilized number n_s. The figure implies that, the Quad8 shows better performance than Quad4, since the Quad8's displacement results are stable no matter the constraint ratio in optimal range or not. And the Quad4's displacement errors increase as soon as the $n_p > n_s$. However, both Quad4's and Quad8's pressure error immediately increase while their constraint ratios are out of optimal range, and Quad8 still have better results than Quad4. Figure 7is the strain and pressure error convergence comparisons for this cantilever beam problem, in which, except Quad8–RK($r = 2$) for strain error, all formulations with traditional constraint ratio of $r = 2$ cannot ensure the optimal error convergence rates. The proposed mixed formulations with $r = r_{opt}$ can maintain the optimal error convergence ratio and show a better accuracy.

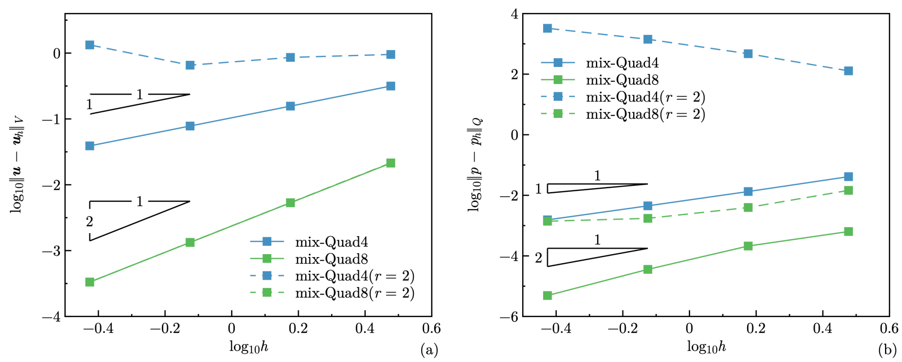

Figure 7: Error convergence study for cantilever beam problem: (a) Strain, (b) Pressure

5.2. Plate with hole problem

Consider an infinite plate with a hole centered at the origin, as shown in Figure 9, and at the infinity towards x–direction subjected an uniform traction $T = 1000$. The geometric and material parameters for this problem is that the ratio of the hole $a = 1$, Young's modulus $E = 3 \times 10^6$ and Poisson's ratio $\nu = 0.5 - 10^{-8}$. The analytical solution of this problem refers the Michell solution [51] as:

$$\begin{cases} u_x(r,\theta) = \dfrac{Ta}{8\mu}\left(\dfrac{r}{a}(k+1)\cos\theta - \dfrac{2a^3}{r^3}\cos 3\theta + \dfrac{2a}{r}((1+k)\cos\theta + \cos 3\theta)\right) \\ u_y(r,\theta) = \dfrac{Ta}{8\mu}\left(\dfrac{r}{a}(k-3)\sin\theta - \dfrac{2a^3}{r^3}\sin 3\theta + \dfrac{2a}{r}((1-k)\sin\theta + \sin 3\theta)\right) \end{cases} \tag{61}$$

in which $k = \frac{3-\nu}{1+\nu}$, $\mu = \frac{E}{2(1+\nu)}$. And the stress components are given by:

$$\begin{cases} \sigma_{xx} = T\left(1 - \dfrac{a^2}{r^2}(\dfrac{3}{2}\cos 2\theta + \cos 4\theta) + \dfrac{3a^4}{2r^4}\cos 4\theta\right) \\ \sigma_{yy} = -T\left(\dfrac{a^2}{r^2}(\dfrac{1}{2}\cos 2\theta - \cos 4\theta) + \dfrac{3a^4}{2r^4}\cos 4\theta\right) \\ \sigma_{xy} = -T\left(\dfrac{a^2}{r^2}(\dfrac{1}{2}\sin 2\theta + \sin 4\theta) - \dfrac{3a^4}{2r^4}\sin 4\theta\right) \end{cases} \tag{62}$$

According to the symmetry property of this problem, only quarter model with length $b = 5$ is considered as shown in Figure 9. The displacement is discretized by 3–node and 6–node triangular elements with 81, 299, 1089 and 4225 nodes. The corresponding linear and quadratic meshfree formulations are employed for pressure discretization, and the characterized support sizes are chosen as 1.5 and 2.5 respectively. Figure 10studies the relationship between strain, pressure errors and n_p, unlike the quadrilateral element case in Section 5.1, the quadaratic Tri6–RK shows worse results while the constraint ratio out of the optimal range. And Tri3–RK exhibits less sensitivity in strain error than Tri6–RK, but its error is increasing while the n_p goes up. Both Tri3–RK and Tri6–RK with constraint ratio under optimal range performance an acceptable result. The corresponding error convergence study is presented in Figure 11, only Tri3–RK with $r = 2$ shows a comparable result with the optimal one with $r = r_{opt}$, the other formulations with traditional constraint ratio show lower accuracy and error convergence rate.

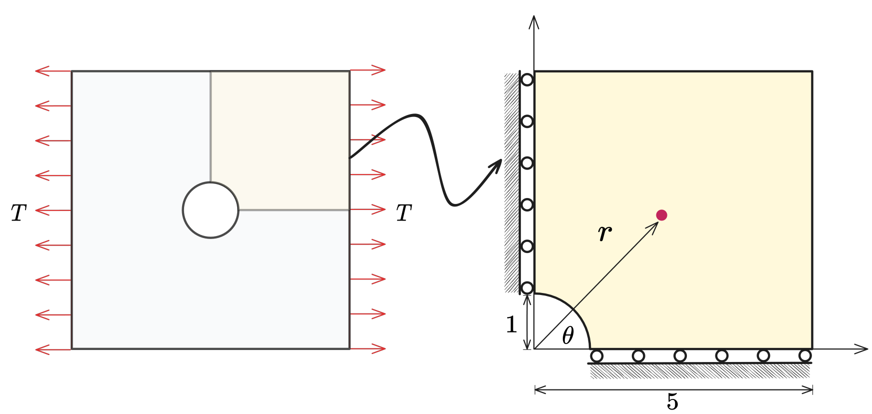

Figure 9: Illustration of plate with hole problem

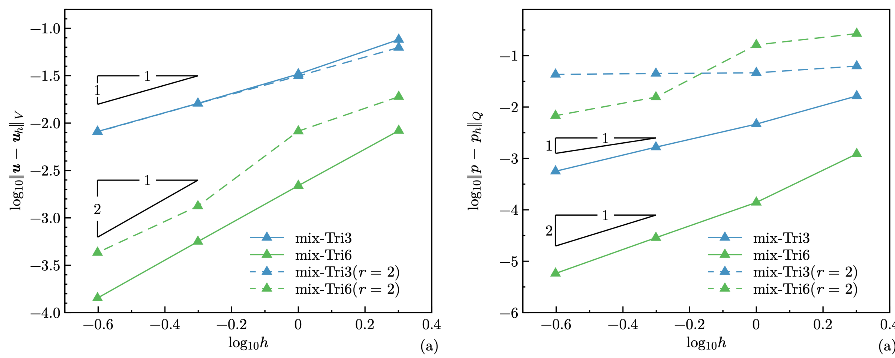

Figure 11: Error convergence study for plate with a hole problem: (a) Strain, (b) Pressure

5.3. Cook membrane problem

The cook membrane problem [12] is used herein for stability analysis of pressure. The geometry of this problem is shown in Figure 12, in which the left hand side is fixed and the right hand side subjects a concentrated force in y–direction.

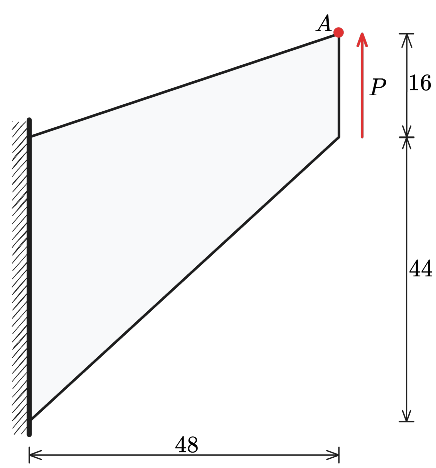

Figure 12: Illustration of cook membrane problem

5.4. Block with pressure problem

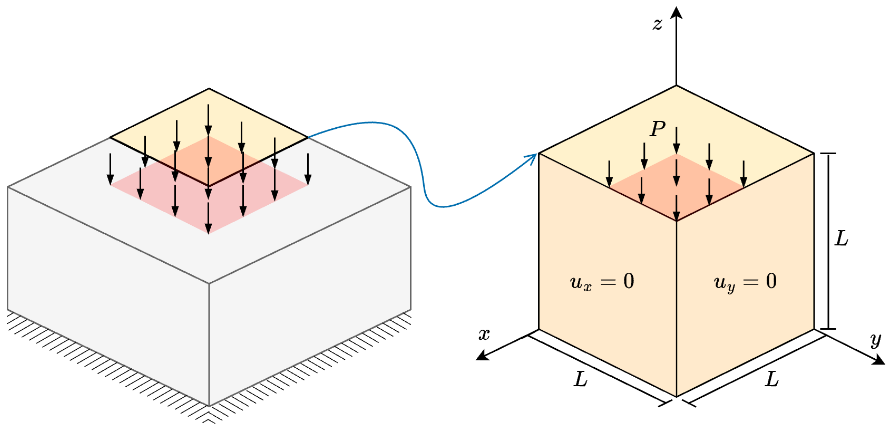

Figure 16: Illustration of block under compression problem

6. Conculsion

This paper proposes a novel optimal constraint ratio derived from the inf-sup condition to address volumetric locking. The optimal constraint ratio requires that, for a given number of displacement DOFs, the number of pressure DOFs should remains below a stabilized number determined by the proposed inf-sup value estimator. For a well-posed nodal distribution, simply counting the displacement and pressure DOFs can determine whether the formulation satisfies the inf-sup condition. Compared to the traditional constraint ratio, the proposed ratio is theoretically grounded in the inf-sup condition and thus is more precise.

To implement this constraint ratio, a mixed finite element (FE) and meshfree formulation is developed. Displacements are discretized using 3-node and 6-node triangular elements, 4-node and 8-node quadrilateral elements in 2D, and 4-node tetrahedral and 8-node hexahedral elements in 3D. Correspondingly, linear and quadratic reproducing kernel meshfree approximations are used for pressure discretization. The reproducing kernel approximation equips globally smooth shape functions, allowing arbitrary pressure DOF placement without the limit of element.

Inf-sup tests for mixed FE-meshfree formulations with different constraint ratios verify the effectiveness of the proposed inf-sup value estimator. For efficiency and ease of implementation, the final nodal distribution scheme selects every other displacement node as a pressure node, ensuring the optimal constraint ratio and satisfying the inf-sup condition.

A series of 2D and 3D incompressible elasticity examples demonstrate the effectiveness of the proposed mixed formulation. Results show that formulations with the optimal constraint ratio yield accurate displacement and pressure solutions. When the constraint ratio exceeds the optimal value, errors rise sharply to unacceptable levels, with the 8-node quadrilateral element being the only exception that maintains good displacement accuracy. Error convergence studies and pressure contour plots further confirm that mixed formulations with the optimal constraint ratio achieve optimal convergence rates and effectively suppress pressure oscillations.

References

[1] F. Brezzi, M. Fortin, Mixed and Hybrid Finite Element Methods, Vol. 15 of Springer Series in Computational Mathematics, Springer, New York, NY, 1991.

[2] T. J. Hughes, The Finite Element Method: Linear Static and Dynamic Finite Element Analysis, Prentice Hall, New Jersey, 2000.

[3] I. Babuška, R. Narasimhan, The Babuška-Brezzi condition and the patch test: An example, Computer Methods in Applied Mechanics and Engineering 140 (1997) 183–199.

[4] K. J. Bathe, Finite Element Procedures, Prentice Hall, Englewood Cliffs, New Jersey, 1996.

[5] D. S. Malkus, Eigenproblems associated with the discrete LBB condition for incompressible finite elements, International Journal of Engineering Science 19 (1981) 1299–1310.

[6] D. Chapelle, K. J. Bathe, The inf-sup test, Computers & Structures 47 (1993) 537–545.

[7] F. Brezzi, K. J. Bathe, Studies of finite element procedures the inf-sup condition equivalent forms and applications.

[8] D. Gallistl, Rayleigh–Ritz approximation of the inf-sup constant for the divergence, Mathematics of Computation 88 (2019) 73–89.

[9] P. Hood, C. Taylor, Navier-Stokes equations using mixed interpolation, Finite element methods in flow problems (1974) 121–132.

[10] D. S. Malkus, T. J. Hughes, Mixed finite element methods - Reduced and selective integration techniques: A unification of concepts, Computer Methods in Applied Mechanics and Engineering 15 (1978) 63–81.

[11] T. Shilt, R. Deshmukh, J. J. McNamara, P. J. O'Hara, Solution of nearly incompressible field problems using a generalized finite element approach, Computer Methods in Applied Mechanics and Engineering 368 (2020) 113165.

[12] J. C. Simo, M. S. Rifai, A class of mixed assumed strain methods and the method of incompatible modes, International Journal for Numerical Methods in Engineering 29 (1990) 1595–1638.

[13] M. Broccardo, M. Micheloni, P. Krysl, Assumed-deformation gradient finite elements with nodal integration for nearly incompressible large deformation analysis, International Journal for Numerical Methods in Engineering 78 (2009) 1113–1134.

[14] W. M. Coombs, T. J. Charlton, M. Cortis, C. E. Augarde, Overcoming volumetric locking in material point methods, Computer Methods in Applied Mechanics and Engineering 333 (2018) 1–21.

[15] S. Saloustros, M. Cervera, S. Kim, M. Chiumenti, Accurate and locking-free analysis of beams, plates and shells using solid elements, Computational Mechanics (Jan. 2021).

[16] C. Rodriguez, T.-H. Huang, A variationally consistent reproducing kernel enhanced material point method and its applications to incompressible materials, Computational Mechanics (2023) 1–20.

[17] J. Simo, R. Taylor, K. Pister, Variational and projection methods for the volume constraint in finite deformation elasto-plasticity, Computer Methods in Applied Mechanics and Engineering 51 (1985) 177–208.

[18] C. R. Dohrmann, P. B. Bochev, A stabilized finite element method for the Stokes problem based on polynomial pressure projections, International Journal for Numerical Methods in Fluids 46 (2004) 183–201.

[19] C. Lovadina, F. Auricchio, On the enhanced strain technique for elasticity problems, Computers & Structures 81 (2003) 777–787.

[20] K.-J. Bathe, The inf–sup condition and its evaluation for mixed finite element methods, Computers & Structures 79 (2001) 243–252.

[21] T. J. R. Hughes, Multiscale phenomena: Green's functions, the Dirichlet-to-Neumann formulation, subgrid scale models, bubbles and the origins of stabilized methods, Computer Methods in Applied Mechanics and Engineering 127 (1995) 387–401.

[22] A. Masud, K. Xia, A Stabilized MixedFinite Element Method for Nearly IncompressibleElasticity, Journal of Applied Mechanics 72 (2005) 711–720.

[23] R. Rossi, R. Zorrilla, R. Codina, A stabilised displacement-volumetric strain formulation for nearly incompressible and anisotropic materials, Computer Methods in Applied Mechanics and Engineering 377 (2021) 113701.

[24] E. Karabelas, M. A. F. Gsell, G. Haase, G. Plank, C. M. Augustin, An accurate, robust, and efficient finite element framework with applications to anisotropic, nearly and fully incompressible elasticity, Computer Methods in Applied Mechanics and Engineering 394 (2022) 114887.

[25] T. J. R. Hughes, L. P. Franca, M. Balestra, A new finite element formulation for computational fluid dynamics: V. Circumventing the babuška-brezzi condition: A stable Petrov-Galerkin formulation of the stokes problem accommodating equal-order interpolations, Computer Methods in Applied Mechanics and Engineering 59 (1986) 85–99.

[26] D. N. Arnold, F. Brezzi, M. Fortin, A stable finite element for the Stokes equations, CALCOLO 21 (1984) 337–344.

[27] F. Auricchio, L. Beirão da Veiga, C. Lovadina, A. Reali, A stability study of some mixed finite elements for large deformation elasticity problems, Computer Methods in Applied Mechanics and Engineering 194 (2005) 1075–1092.

[28] A. Quarteroni, A. Valli, Numerical Approximation of Partial Differential Equations, Springer Series in Computational Mathematics, Springer, Berlin, 1994.

[29] M. Crouzeix, P. Raviart, Conforming and nonconforming finite element methods for solving the stationary Stokes equations I, Revue française d'automatique informatique recherche opérationnelle. Mathématique 7 (1973) 33–75.

[30] U. Brink, E. Stein, On some mixed finite element methods for incompressible and nearly incompressible finite elasticity, Computational Mechanics 19 (1996) 105–119.

[31] T. Belytschko, Y. Y. Lu, L. Gu, Element-free Galerkin methods, International Journal for Numerical Methods in Engineering 37 (1994) 229–256.

[32] W. K. Liu, S. Jun, Y. F. Zhang, Reproducing kernel particle methods, International Journal for Numerical Methods in Fluids 20 (1995) 1081–1106.

[33] S. W. Chi, J. S. Chen, H. Y. Hu, A weighted collocation on the strong form with mixed radial basis approximations for incompressible linear elasticity, Computational Mechanics 53 (2014) 309–324.

[34] L. Wang, Z. Qian, Y. Zhou, Y. Peng, A weighted meshfree collocation method for incompressible flows using radial basis functions, Journal of Computational Physics 401 (2020) 108964.

[35] A. Ortiz-Bernardin, M. Puso, N. Sukumar, Improved robustness for nearly-incompressible large deformation meshfree simulations on Delaunay tessellations, Computer Methods in Applied Mechanics and Engineering 293 (2015) 348–374.

[36] T. J. Hughes, J. A. Cottrell, Y. Bazilevs, Isogeometric analysis: CAD, finite elements, NURBS, exact geometry and mesh refinement, Computer Methods in Applied Mechanics and Engineering 194 (2005) 4135–4195.

[37] F. Auricchio, L. Beirão da Veiga, C. Lovadina, A. Reali, The importance of the exact satisfaction of the incompressibility constraint in nonlinear elasticity: Mixed FEMs versus NURBS-based approximations, Computer Methods in Applied Mechanics and Engineering 199 (2010) 314–323.

[38] A. Huerta, S. Fernández-Méndez, Locking in the incompressible limit for the element-free Galerkin method, International Journal for Numerical Methods in Engineering 51 (2001) 1361–1383.

[39] J. Dolbow, T. Belytschko, Volumetric locking in the element free Galerkin method, International Journal for Numerical Methods in Engineering 46 (1999) 925–942.

[40] G. Moutsanidis, J. J. Koester, M. R. Tupek, J.-S. Chen, Y. Bazilevs, Treatment of near-incompressibility in meshfree and immersed-particle methods, Computational Particle Mechanics 7 (2020) 309–327.

[41] G. Moutsanidis, W. Li, Y. Bazilevs, Reduced quadrature for FEM, IGA and meshfree methods, Computer Methods in Applied Mechanics and Engineering 373 (2021) 113521.

[42] Z.-Y. Wang, Y.-F. Jin, Z.-Y. Yin, Y.-Z. Wang, Overcoming volumetric locking in stable node-based smoothed particle finite element method with cubic bubble function and selective integration, International Journal for Numerical Methods in Engineering 123 (2022) 6148–6169.

[43] J. S. Chen, S. Yoon, H. P. Wang, W. K. Liu, An improved reproducing kernel particle method for nearly incompressible finite elasticity, Computer Methods in Applied Mechanics and Engineering 181 (2000) 117–145.

[44] C. M. Goh, P. M. F. Nielsen, M. P. Nash, A stabilised mixed meshfree method for incompressible media: Application to linear elasticity and Stokes flow, Computer Methods in Applied Mechanics and Engineering 329 (2018) 575–598.

[45] D. S. Bombarde, M. Agrawal, S. S. Gautam, A. Nandy, Hellinger–Reissner principle based stress–displacement formulation for three-dimensional isogeometric analysis in linear elasticity, Computer Methods in Applied Mechanics and Engineering 394 (2022) 114920.

[46] A. Huerta, Y. Vidal, P. Villon, Pseudo-divergence-free element free Galerkin method for incompressible fluid flow, Computer Methods in Applied Mechanics and Engineering 193 (2004) 1119–1136.

[47] C. Wu, W. Hu, J. Chen, A meshfree-enriched finite element method for compressible and near-incompressible elasticity, International Journal for Numerical Methods in Engineering 90 (2012) 882–914.

[48] E. Stein, R. de Borst, T. J. R. Hughes (Eds.), Encyclopedia of Computational Mechanics, John Wiley, Chichester, West Sussex, 2004.

[49] I. Babuška, J. Osborn, Eigenvalue Problems, in: Handbook of Numerical Analysis, Vol. 2 of Finite Element Methods (Part 1), Elsevier, 1991, pp. 641–787.

[50] K. Yosida, Functional Analysis, 6th Edition, Classics in Mathematics, Springer-Verlag, Berlin Heidelberg, 1995.

[51] S. Timoshenko, J. Goodier, Theory of Elasticity, Engineering Mechanics Series, McGraw-Hill, 1969.

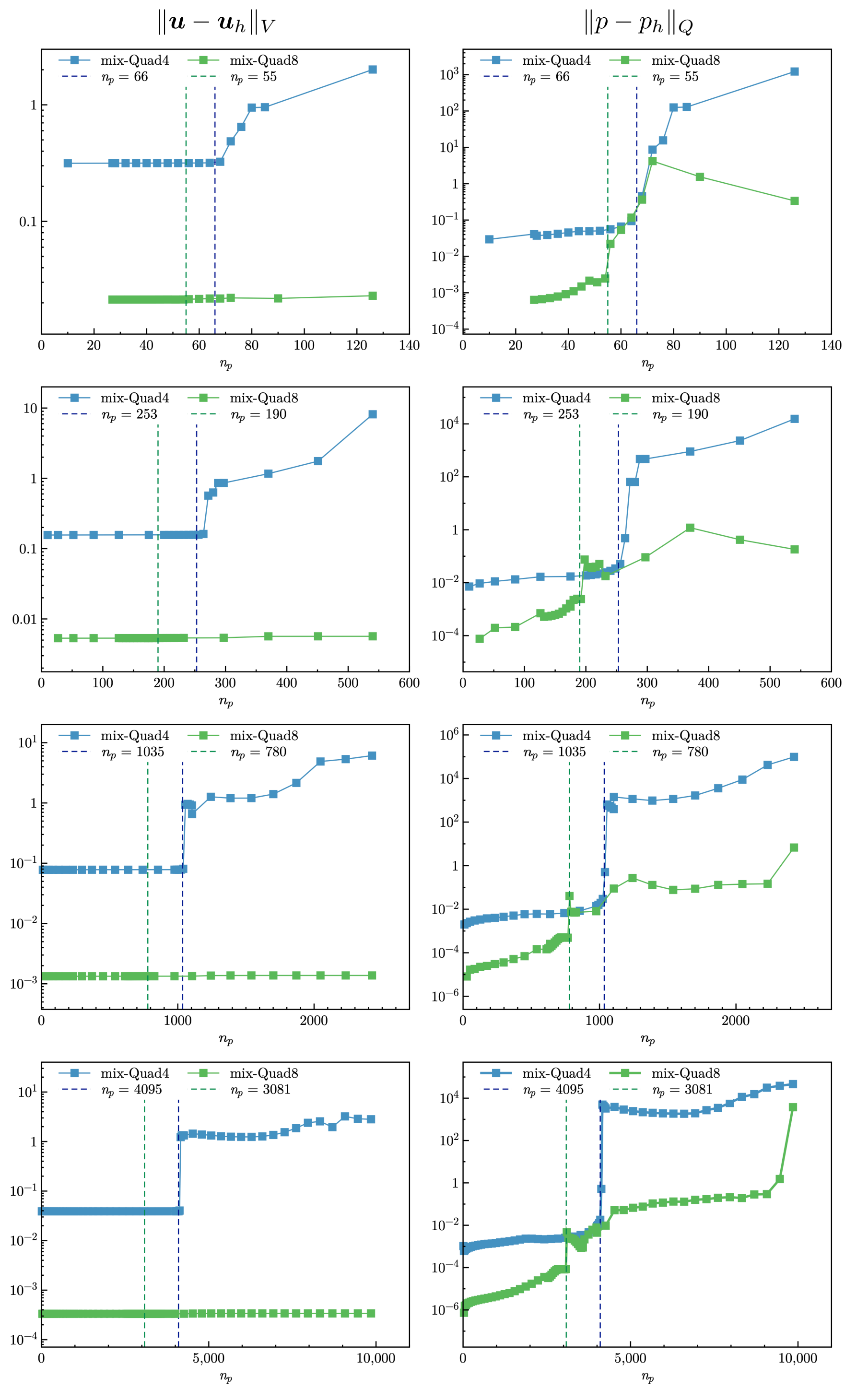

Figure 6: Strain and pressures errors v.s. n_p for cantilever beam problem

Figure 8: Contour plots of cook membrane problem

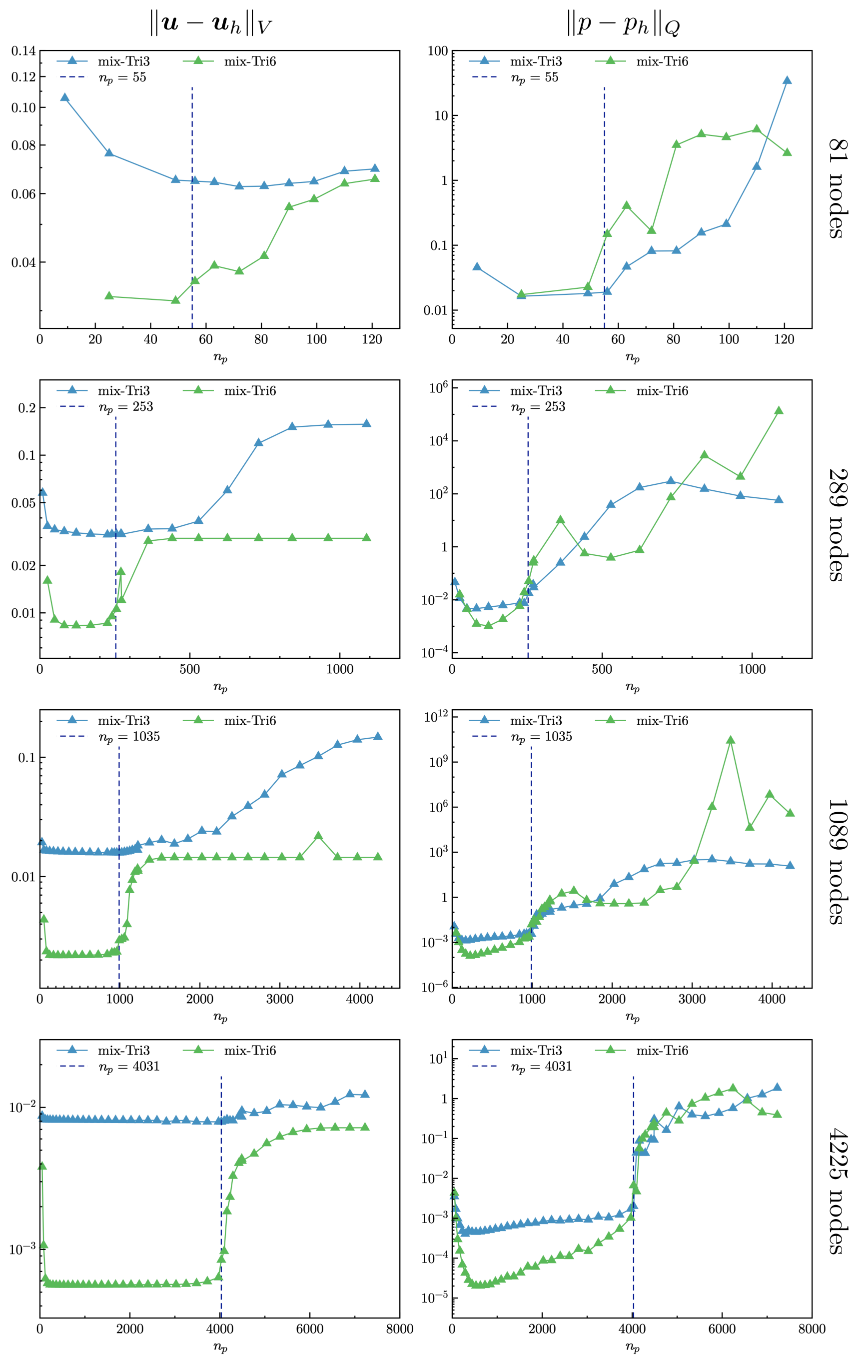

Figure 10: Strain and pressures errors v.s. n_p for plate with hole problem

Figure 13: Illustration of block under compression problem

Figure 14: Convergence comparison of block under compression problem

Figure 15: Contour plots of block under compression problem